Supporting Information for "On the tropical cyclone integrated kinetic energy balance"

A. Avenas[1], A. Mouche[1], J. Knaff[2], X. Carton[1], B. Chapron[1]

[1]Ifremer, Univ. Brest, CNRS, IRD, Laboratoire d'Océanographie Physique et Spatiale (LOPS), IUEM, F-29280, Plouzané, France

[2]NOAA/NESDIS Regional and Mesoscale Meteorological Branch, Fort Collins, Colorado

Contents of this file

1. Texts S1 to S5

2. Figures S1 to S2

Text S1: SAR observations

High spatial resolution observations of the ocean surface are obtained with spaceborne SAR. The SAR instrument operates at 5.4 GHz (C-band) and receives the signal backscattered by the ocean surface in both co- and cross-polarization. This allows to estimate ocean surface wind speeds under TC conditions, including at very high wind speeds and in the near-core region (A. A. Mouche et al., 2017; A. Mouche et al., 2019; Combot et al., 2020).

Because SAR wide-swath acquisitions cannot be continuously performed over oceans, they have to be triggered based on track forecasts to anticipate when the sensor will

———

June 17, 2024, 7:54am

overpass a TC. Since 2016, more than $\sim$500 acquisitions over TCs from ESA Sentinel-1A and Sentinel-1B and Canadian Space Agency Radarsat-2 missions were gathered as part of the Satellite Hurricane Observation Campaign (SHOC).

The wind product derived by A. A. Mouche et al. (2017) has a 3 km spatial resolution with a 1 km grid spacing and is interpolated on a regular polar grid based on the TC center (see appendix in Vinour, Jullien, Mouche, Combot, and Mangeas (2021)). For each SAR case, a wind profile is then obtained by averaging the wind estimates on all azimuths. Typical standard deviations of wind speed along the azimuthal direction are displayed in Figs. 1c, d from the main text (green shaded areas). In addition, a certain number of SAR cases have been discarded on a qualitative basis, $e.g$ when the detected TC center was judged to be wrong, or when the SAR file contained corrupted pixel values.

To restrain the analysis to well-formed systems, after estimating the SAR parameters (see below), we select only SAR cases for which $V_{max} > 20$ m/s, $R_{max} < 150$ km, and absolute latitude $< 30°$. Based on best-track data, we also ensure that, for each SAR case, the distance to closest land from TC center is greater than SAR-derived R_{34} estimate.

Text S2: Parameters estimation

In order to reduce the problem dimension, scalar parameters characterizing the TC axisymmetric wind profiles are computed based on the high spatial resolution SAR total wind estimates. These include the maximum intensity amplitude (V_{max}) and location (R_{max}), the Coriolis parameter (f) based on the TC center latitude, the radius of significant upward motions (R_+) defined by Eq. 4 from the main text and the corresponding wind speed (V_+). The radius of zero outflow velocity (R_0) is then derived based on (V_{max},

R_{max}, f) and the corresponding wind speed (V_0) is further computed on the SAR axisymmetric wind profile.

To quantify the surface wind decay, a Holland wind parametric profile and the corresponding B parameter are used (Holland, 1980). Based on gradient wind balance, Holland parametric wind profile is not necessarily suited for surface wind profiles with nonzero wind speeds at the TC center, well captured using SAR observations. A complementary degree of freedom is thus added to minimize the impact of these nonzero wind speeds on the resulting B values. For each SAR wind profile, a modified Holland parametric profile

$$V_{Holland}(r) = V_{min} + \sqrt{(V_{max} - V_{min})^2 (\frac{R_{max}}{r})^{B_s} e^{1-(\frac{R_{max}}{r})^{B_s}} + (\frac{rf}{2})^2} - \frac{rf}{2} \qquad (1)$$

is adjusted to each SAR azimuthally-averaged wind profile using the full extent of the wind profile and estimating solutions for V_{min}, V_{max}, R_{max} and B_s via least squares, while f was fixed by the TC center estimated on the SAR acquisition. The modified Holland parameter B_s is used to quantify the surface wind decay for each SAR azimuthally-averaged wind profile.

Lastly, note that to estimate R_+, an estimate of ω_z is first needed, which requires to compute a radial derivative. Radial derivatives are difficult to estimate directly on SAR observations because of local jumps in the wind speed estimates implied by high spatial resolution, even though a substantial part of this noise has been smoothed by azimuthally-averaging. Thus, the adjusted parametric profiles are used to estimate ω_z, and then R_+ using Eq. 4 from the main text.

Text S3: Kinetic energy balance

June 17, 2024, 7:54am

Here, we derive Eq. 2 from the main text, starting with the primitive equations and following the developments of (Kalashnik, 1994). While air density may be assumed constant, we first treat the more general case of anelastic approximation, where air density is decomposed as $\rho =: \bar{\rho}(z) + \rho'$ with $\rho' \ll \bar{\rho}(z)$. Pressure then reduces to $P =: \bar{P}(z) + P'$ with $P' \ll \bar{P}(z)$ and potential temperature to $\theta =: \bar{\theta}(z) + \theta'$ with $\theta' \ll \bar{\theta}(z)$. Then, the equations of conservation of tangential momentum, gradient wind and hydrostatic balance, continuity, and conservation of energy reduce to

$$\frac{\partial v}{\partial t} + u\frac{\partial v}{\partial r} + w\frac{\partial v}{\partial z} + \frac{uv}{r} + fu = 0 \tag{2}$$

$$\frac{v^2}{r} + fv = \frac{\partial \Phi}{\partial r} \tag{3}$$

$$\frac{\partial \Phi}{\partial z} = g\tilde{\theta} \tag{4}$$

$$\frac{1}{r}\frac{\partial}{\partial r}(ru) + \frac{1}{\bar{\rho}}\frac{\partial}{\partial z}(\bar{\rho}w) = 0 \tag{5}$$

$$\frac{\partial \tilde{\theta}}{\partial t} + u\frac{\partial \tilde{\theta}}{\partial r} + w\frac{\partial \tilde{\theta}}{\partial z} + \Gamma w = \frac{Q}{C_p\bar{T}} \tag{6}$$

with u, v, and w the radial, azimuthal and vertical components of velocity, r, z the radial and vertical coordinates, t the time, Q the heat source and C_p the heat capacity. The notations are $\Phi := \frac{P'}{\bar{\rho}}$, $\tilde{\theta} := \frac{\theta'}{\bar{\theta}}$, $\Gamma := \frac{1}{\bar{\theta}}\frac{d\bar{\theta}}{dz}$.

The volume on which these equations are considered is defined by $0 \leq r \leq R_0$ and $0 \leq z \leq H$, where $z = 0$ corresponds to the top of the boundary layer. It is also assumed

that $w(z = H) = 0$ at all radii and that $v(r = R_0) = 0$ at all levels. A schematic illustration of the TC system considered here along with the assumptions used in the present paper is given in Fig. S1.

Momentum sink

First, noting $K := \frac{V^2}{2}$, we multiply Eq. 2 by v and using Eq. 3:

$$\frac{\partial K}{\partial t} + u\frac{\partial K}{\partial r} + w\frac{\partial K}{\partial z} + u\frac{\partial \Phi}{\partial r} = 0 \tag{7}$$

After multiplication by $\bar{\rho}$, Eq. 7 is integrated on the volume $\langle(.)\rangle := \int_0^H \int_0^{R_0} (.)r\,dr\,dz$. The first term of the integrated equation is rewritten as $\frac{\partial}{\partial t}\langle\bar{\rho}K\rangle$.

Before integrating the other terms, we notice that for any variable χ integration by parts and continuity equation yields:

$$\int_0^{R_0} \bar{\rho}ru\frac{\partial \chi}{\partial r}\,dr = \left[\bar{\rho}ru\chi\right]_0^{R_0} - \int_0^{R_0} \chi\frac{\partial(\bar{\rho}ru)}{\partial r}\,dr = \int_0^{R_0} \chi\frac{\partial}{\partial z}(\bar{\rho}rw)\,dr \tag{8}$$

With this result, the second and third terms of Eq. 7 become, after integration

$$\int_0^H \int_0^{R_0} \left(\bar{\rho}ru\frac{\partial K}{\partial r} + \bar{\rho}rw\frac{\partial K}{\partial z}\right)\,dr\,dz = \int_0^H \int_0^{R_0} \left(K\frac{\partial}{\partial z}(\bar{\rho}rw) + \bar{\rho}rw\frac{\partial K}{\partial z}\right)\,dr\,dz$$
$$= \int_0^{R_0} \left[\bar{\rho}rwK\right]_{z=0}\,dr \tag{9}$$

where we used Eq. 8 and $w(z = H) = 0$. Finally, the last integrated term of Eq. 7 is

$$\int_0^H \int_0^{R_0} \bar{\rho}ru\frac{\partial \Phi}{\partial r}\,dr\,dz = \int_0^H \int_0^{R_0} \Phi\frac{\partial}{\partial z}(\bar{\rho}rw)\,dr\,dz \tag{10}$$

By permuting the integrals, integrating by parts, and using $w(z = H) = 0$, we further rearrange:

:

$$\int_0^H \int_0^{R_0} \Phi \frac{\partial}{\partial z}(\bar{\rho}rw)\, dr\, dz = \int_0^{R_0} \left[\bar{\rho}rw\Phi \right]_{z=0} dr - \int_0^H \int_0^{R_0} \bar{\rho}rw \frac{\partial \Phi}{\partial z}\, dr\, dz \qquad (11)$$

where, because of Eq. 4, the last term is simply $g\langle \bar{\rho}w\tilde{\theta} \rangle$.

Using eqs. 9, 11, the integration of Eq. 7 finally yields:

$$\frac{\partial}{\partial t}\langle \bar{\rho}K \rangle - \int_0^{R_0} \left[\bar{\rho}rw(K + \Phi) \right]_{z=0} dr = g\langle \bar{\rho}w\tilde{\theta} \rangle \qquad (12)$$

Using the expression for the Ekman vertical velocity (Eq. 3 from the main text) the second term of Eq. 12 can be written

$$\int_0^{R_0} \left[\bar{\rho}rw(K + \Phi) \right]_{z=0} dr = \int_0^{R_0} \left[\bar{\rho}\frac{d}{dr}\left(\frac{C_d rv^2}{\omega_z + f} \right)(K + \Phi) \right]_{z=0} dr \qquad (13)$$

Before rearranging this term further, we first notice that gradient wind balance (Eq. 3) implies that

$$\frac{\partial}{\partial r}(K + \Phi) = v(\omega_z + f) \qquad (14)$$

Integrating Eq. 13 by parts to use Eq. 14, then substituting for this expression in Eq. 12 yields

$$\frac{\partial}{\partial t}\langle \bar{\rho}K \rangle + \int_0^{R_0} \left[\bar{\rho}C_d rv^3 \right]_{z=0} dr = g\langle \bar{\rho}w\tilde{\theta} \rangle \qquad (15)$$

Heat source

Now, Eq. 6 is integrated on the volume $\langle\langle (.) \rangle\rangle := \int_0^H \int_0^z \int_0^{R_0} (.)r\, dr\, dz\, dz$, after multiplication by $\bar{\rho}$. The first term of the equation becomes $\frac{\partial}{\partial t}\langle\langle \bar{\rho}\tilde{\theta} \rangle\rangle$.

When summing the second and third terms of the integrated equation, we obtain:

$$\int_0^H \int_0^z \int_0^{R_0} \left(\bar{\rho} r u \frac{\partial \tilde{\theta}}{\partial r} + \bar{\rho} r w \frac{\partial \tilde{\theta}}{\partial z} \right) dr \, dz \, dz = \int_0^H \int_0^z \int_0^{R_0} \left(\tilde{\theta} \frac{\partial}{\partial z} (\bar{\rho} r w) + \bar{\rho} r w \frac{\partial \tilde{\theta}}{\partial z} \right) dr \, dz \, dz$$

$$= \int_0^H \int_0^{R_0} \left[\bar{\rho} r w \tilde{\theta} \right]_0^z dr \, dz$$

$$= \langle \bar{\rho} w \tilde{\theta} \rangle - H \int_0^{R_0} \left[\bar{\rho} r w \tilde{\theta} \right]_{z=0} dr$$

$$(16)$$

where we used Eq. 8. Next, the stratification term is integrated as

$$\int_0^H \int_0^z \int_0^{R_0} \bar{\rho} r w \Gamma \, dr \, dz \, dz = \int_0^z \int_0^{R_0} \left(\left[\bar{\rho} r w \ln(\bar{\theta}) \right]_0^H - \int_0^H \frac{\partial}{\partial z} (\bar{\rho} r w) \ln(\bar{\theta}) \, dz \right) dr \, dz$$

$$= 0$$

$$(17)$$

where, in the first raw, the first term is zero at $z = H$ because $w(z = H) = 0$ and zero at $z = 0$ because $\int_0^{R_0} r w_E \, dr = 0$, while the second term is zero by applying the continuity equation and recalling that $\ln(\bar{\theta})$ is independent from r.

In order to integrate the heat source term, Q must be prescribed. Here it is taken as proportional to the Ekman pumping w_E (Eq. 3 from the main text) in the region of significant vertical motions and zero elsewhere

$$Q(r, z) = \begin{cases} \beta(z) q_b L w_E(r), & r \le R_+ \\ 0 & r > R_+ \end{cases} \quad (18)$$

with $\beta(z)$ a vertical heat profile which is normalized on the interval $[0, H]$ and has the dimension of inverse length, q_b the specific humidity in the boundary layer and L the latent heat of condensation.

Finally, integrating the heat source term yields

$$\int_0^H \int_0^z \int_0^{R_0} \frac{\bar{\rho} r Q}{C_p \bar{\bar{T}}} \, dr \, dz \, dz = \int_0^H \int_0^z \frac{\bar{\rho} \beta q_b L}{C_p \bar{\bar{T}}} \int_0^{R_0} r w_E \, dr \, dz \, dz$$

$$= \alpha \left[\frac{C_d r v^2}{\omega_z + f} \right]_{z=0, \ r=R_+} \tag{19}$$

where we defined

$$\alpha := \frac{q_b L}{C_p} \int_0^H \int_0^z \frac{\bar{\rho}(z) \beta(z)}{\bar{T}(z)} \, dz \, dz \tag{20}$$

In the end, integration of Eq. 6 yields, after multiplication by g:

$$g \frac{\partial}{\partial t} \langle\langle \bar{\rho} \theta \rangle\rangle + g \langle \bar{\rho} w \theta \rangle = g \alpha \left[\frac{C_d r v^2}{\omega_z + f} \right]_{z=0, \ r=R_+} \tag{21}$$

where we further neglected the heat fluxes $H \int_0^{R_0} \left[\bar{\rho} r w \tilde{\theta} \right]_{z=0} \, dr$ in Eq. 16.

Steady-state balance

Equations 15 and 21 are valid under the anelastic approximation, $i.e$ when ρ is everywhere not far from the average vertical profile $\bar{\rho}(z)$. To further simplify, we now consider the case of constant air density $\bar{\rho}(z) \equiv \bar{\rho}_0$. Then, in steady-state, Eqs. 15, 21 can be combined to obtain:

$$\int_0^{R_0} \left[C_d r v^3 \right]_{z=0} \, dr = U_c^2 \left[\frac{C_d r v^2}{\omega_z + f} \right]_{z=0, \ r=R_+} \tag{22}$$

with $U_c := \sqrt{\frac{g \alpha}{\bar{\rho}_0}}$ is homogeneous to a velocity.

Characteristic velocity

In order to estimate the characteristic velocity U_c, we may assume that the heating is concentrated in the lowest layers of the TC, $e.g$ in the boundary layer. Further assuming

that the temperature in the boundary layer is a constant $\bar{T}_0$, the characteristic velocity becomes

$$U_c^2 = \frac{g q_b L \beta_0}{C_p \bar{T}_0} \tag{23}$$

where $\beta_0 := \int_0^H \int_0^z \beta(z)\,dz\,dz$. We may use an analytical form for $\beta(z)$, for instance $\beta(z) := \frac{e^{-\frac{z}{\delta}}}{\delta(1-e^{-\frac{H}{\delta}})}$, which leads to $\beta_0 = \frac{H}{1-e^{-\frac{H}{\delta}}} - \delta$. To further estimate U_c, we need an estimate of δ, which should correspond to the boundary layer height. By prescribing $\delta \sim \frac{H}{20}$ (corresponding for instance to a TC that is ~ 10 km high and whose boundary layer is ~ 0.5 km high), we find $\beta_0 \sim \frac{H}{19}$, which we can use along with Eq. 12 from the main text to rearrange Eq. 23. We obtain

$$U_c^2 = \frac{V_{max}^2 q_b L}{19 C_p \bar{T}_0 \frac{\Delta\theta}{\theta_0}} \tag{24}$$

Typical values for the remaining parameters are $q_b \sim 20$ g/kg, $L \sim 2.5 \times 10^6$ J/kg, $C_p \sim 1 \times 10^3$ J/kg/K, and $\bar{T}_0 \sim 300$ K. For $V_{max} \sim 34$ m/s, the average V_{max} for the most steady IKE cases of the SAR database (black stars in Fig. 3 from the main text), we find $U_c \sim 32$ m/s.

Text S4: Wind structure parameters

The characteristic radii R_0 and R_+ may be extracted from the 178 wind profiles of the SAR database. Figure S2 represents the ratio $\frac{R_+}{R_{max}}$ as a function of Ro_{max} for all these cases. A relation of proportionality between this ratio and Ro_{max} is apparent. In addition, for a given Ro_{max}, higher B_s values (*i.e* increased surface wind decay) decrease the ratio $\frac{R_+}{R_{max}}$ (see for instance Lane and Meranti in Fig. S2).

The controlling effect of Ro_{max} and B_s on the wind structure may then be interpreted in terms of distances of R_0 and R_+ from the TC center in units of R_{max} because Ro_{max} increases with both $\frac{R_+}{R_{max}}$ (Fig. S2) and $\frac{R_0}{R_{max}}$ (Eq. 5 from the main text) while B_s decreases with $\frac{R_+}{R_{max}}$ (Fig. S2).

Text S5: Best-track data

Time derivatives of TCs intensity ($\frac{\partial V_{max}}{\partial t}$) and outer-size ($\frac{\partial R_{34}}{\partial t}$) are obtained from best-track data. Indeed, direct estimates of these quantities on SAR data only is currently prevented by the limited spatio-temporal sampling of the SAR instruments.

Both $\frac{\partial V_{max}}{\partial t}$ and $\frac{\partial R_{34}}{\partial t}$ are computed from best-track by first averaging V_{max} and R_{34} time series using a four-hour moving window to smooth out noisy values and then computing second order accurate central differences. Then, these two parameters, along with the distance to closest land, are linearly interpolated to each SAR acquisition time.

Lastly, because of varying definitions of the maximum sustained wind speed across the different agencies, we selected only USA agencies (*i.e* National Hurricane Center, Joint Typhoon Warning Center, and Central Pacific Hurricane Center) which all provide the 1-minute maximum sustained wind speed.

References

Combot, C., Mouche, A., Knaff, J., Zhao, Y., Zhao, Y., Vinour, L., . . . Chapron, B. (2020). Extensive high-resolution synthetic aperture radar (sar) data analysis of tropical cyclones: Comparisons with sfmr flights and best track. *Monthly Weather Review, 148*(11), 4545–4563.

Holland, G. J. (1980). An analytic model of the wind and pressure profiles in hurricanes.

Monthly Weather Review, *108*, 1212–1218.

Kalashnik, M. (1994). On the maximum wind velocity in the tropical cyclone. *Izvestiâ Akademii nauk SSSR. Fizika atmosfery i okeana*, *30*(1), 26–30.

Mouche, A., Chapron, B., Knaff, J., Zhao, Y., Zhang, B., & Combot, C. (2019). Copolarized and cross-polarized sar measurements for high-resolution description of major hurricane wind structures: Application to irma category 5 hurricane. *Journal of Geophysical Research: Oceans*, *124*(6), 3905–3922.

Mouche, A. A., Chapron, B., Zhang, B., & Husson, R. (2017). Combined co-and cross-polarized sar measurements under extreme wind conditions. *IEEE Transactions on Geoscience and Remote Sensing*, *55*(12), 6746–6755.

Vinour, L., Jullien, S., Mouche, A., Combot, C., & Mangeas, M. (2021). Observations of tropical cyclone inner-core fine-scale structure, and its link to intensity variations. *Journal of the Atmospheric Sciences*, *78*(11), 3651–3671.
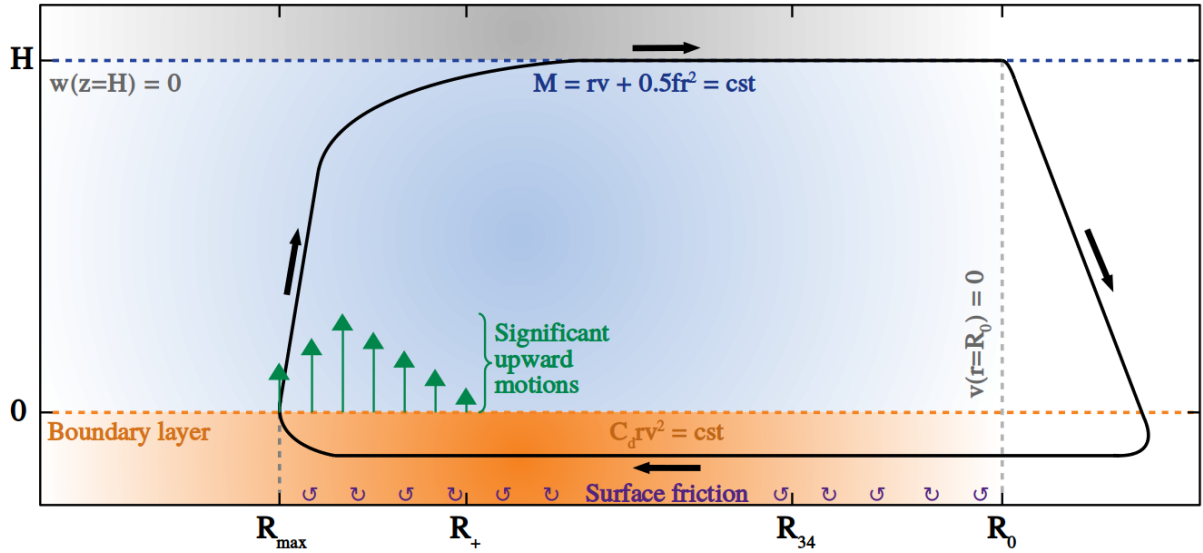
Figure S1. Schematic illustration of the TC system. The meridional circulation (black lines) is represented in a (r, z)-plane, with black arrows indicating the sense of the circulation. In the region of significant upward motions, green arrows represent the vertical velocity at the top of the boundary layer due to Ekman pumping. The radii used in this study are placed in the order given by their average value in the SAR database: $R_{max} \sim 32$ km, $R_+ \sim 57$ km, $R_{34} \sim 139$ km, and $R_0 \sim 216$ km.
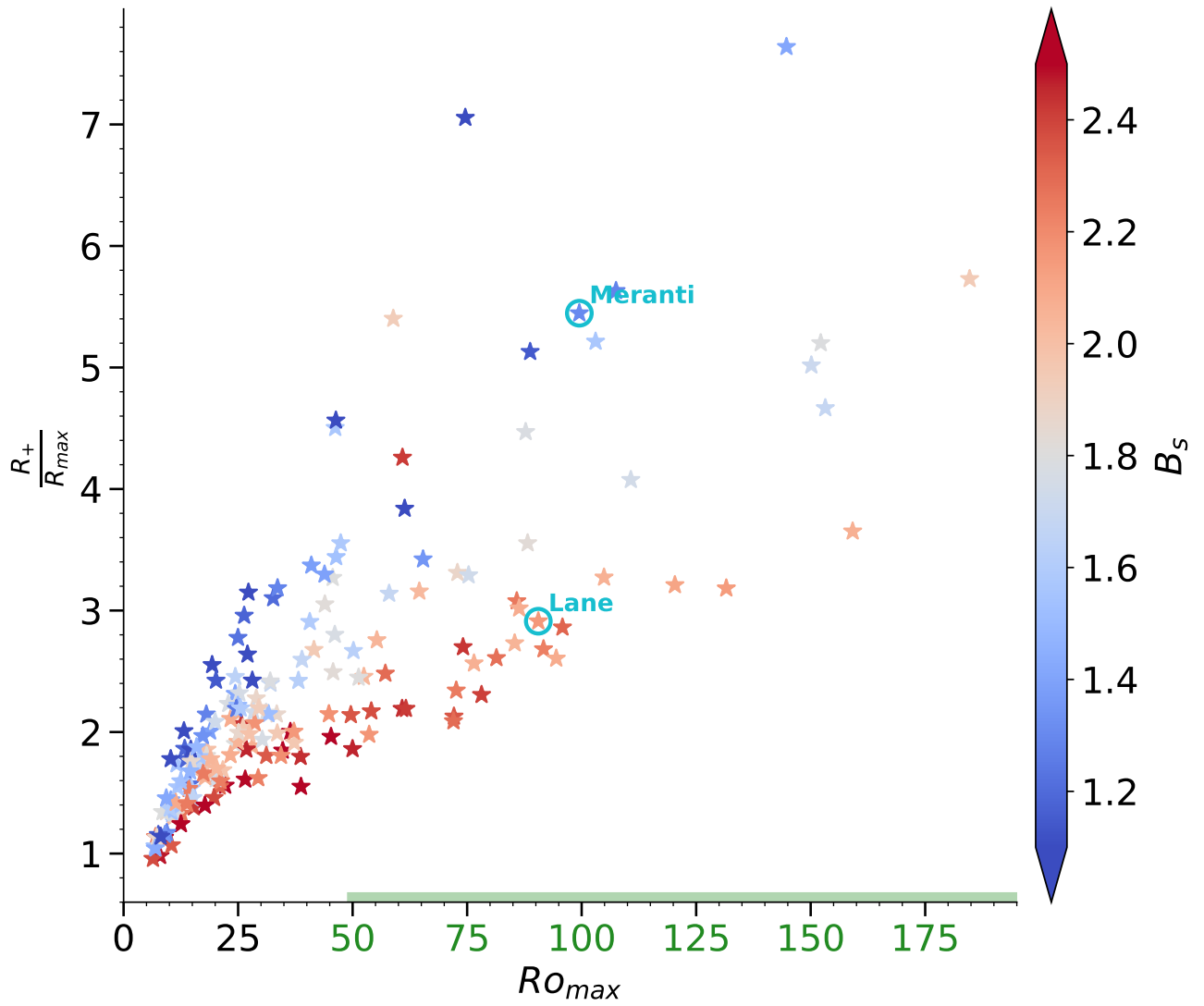
Figure S2. Observed dependency of $\frac{R_+}{R_{max}}$ on Ro_{max} and B_s. Each star represents a SAR observation. The x-axis is shaded in green for $Ro_{max} > 50$.